OPEN ACCESS
IOP Publishing
Nanotechnology

Nanotechnology **35** (2024) 415703 (9pp)
https://doi.org/10.1088/1361-6528/ad5dbd

Mapping and spectroscopy of telecom quantum emitters with confocal laser scanning microscopy

Thomas Descamps[1,*], **Alexandros Bampis**[1], **Maximilien Huet**[1], **Mattias Hammar**[2] and **Val Zwiller**[1,*]

[1] Department of Applied Physics, Royal Institute of Technology, Roslagstullsbacken 21, 10691 Stockholm, Sweden
[2] Department of Electrical Engineering, Royal Institute of Technology, 164 40 Kista, Sweden

E-mail: descamps@kth.se and zwiller@kth.se

Received 12 March 2024, revised 10 June 2024
Accepted for publication 2 July 2024
Published 26 July 2024

Abstract

Efficiently coupling single-photon emitters in the telecommunication C-band that are not deterministically positioned to photonic structures requires both spatial and spectral mapping. This study introduces the photoluminescence mapping of telecom C-band self-assembled quantum dots (QDs) by confocal laser scanning microscopy, a technique previously unexplored in this wavelength range which fulfills these two requirements. We consider the effects of distortions inherent to any imaging system but largely disregarded in prior works to derive accurate coordinates from photoluminescence maps. We obtain a position uncertainty below 11 nm for 10% of the QDs when assuming no distortions, highlighting the potential of the scanning approach. After distortion correction, we found that the previously determined positions are on average shifted by 428 nm from the corrected positions, demonstrating the necessity of this correction for accurate positioning. Then, through error propagation, the position uncertainty for 10% of the QDs increases to 110 nm.

Keywords: quantum dot imaging, confocal laser scanning microscopy, single-photon source, telecom wavelength

1. Introduction

A shared fundamental requirement for two essential technologies in quantum information, namely quantum networks for secure communication [1–3] and on-chip photonic circuits for quantum computing [4, 5], is the need for single-photon emitters. Among various solid-state candidates, semiconductor quantum dots (QDs) emerge as a viable source of pure [6], indistinguishable [2, 7] single-photons as well as entangled photon pairs [1, 8]. While extensively studied with intrinsic emission wavelengths below 1 μm, ongoing efforts aim to extend their emission to the telecommunication O and C band to minimize losses in optical fibers [9]. Yet, the limited brightness of the sources originating from the long QD excitations lifetime and the total internal reflections occurring at the surface of the semiconductor limit their direct use in scaled quantum technologies. These restrictions can be overcome by coupling the emitters to resonant photonic cavities fabricated in the semiconductor matrix [10–12], but deterministic integration is complicated by multiple factors. These include challenges related to the processing of the host material [13, 14] and fabrication imperfections that may cause deviations in the cavity shape, leading to a spectral mismatch

* Authors to whom any correspondence should be addressed.

between the cavity mode and the emitter [15] or limit the quality factor [15, 16]. In addition, surface defects created during nanofabrication can broaden the linewidth of the emitter and introduce spectral wandering [17] and random processes introduced by the growth process further complicate the integration. The latter issue first includes the random distribution of the QDs in the plane perpendicular to the growth direction. Second, fluctuations in their lateral sizes introduce uncertainties in their exact emission properties (emission wavelength and linewidth, fine structure splitting), which can be further exacerbated by local changes in strain and charge environment [18–20]. Consequently, spatial identification and spectral characterization of the QDs become two prerequisites for efficient coupling to the cavity mode. Various mapping techniques have been developed for this purpose: wide-field photoluminescence (PL) imaging [21–23], confocal PL scanning [24], *in-situ* photolithography [25] and *in-situ* electron beam lithography (EBL) [26]. While primarily applied to QDs emitting below 1 μm, these methods are typically a compromise between ease of mapping and processing, availability and final accuracy of the alignment. Their extension to emitters in the telecommunication O- and C- bands has become a technological necessity, but comes with more challenges. On the one hand, the QD excitations tend to be dimmer due to their longer lifetime, requiring longer exposure times. For neutral excitons generated by above-band excitations, previous studies reported lifetimes of approximately 1.29 ns for InAs QDs grown on a metamorphic buffer (MMB) [27] and 1.32 ns for InAs/InP QDs [28], both emitting in the C-band. In comparison, the decay time decreases to about 200 ps for GaAs QDs in nanoholes emitting around 795 nm [29, 30] and about 800 ps for InGaAs/GaAs emitting between 900 and 950 nm [18]. For trions, the lifetime is about 1.55 ns on average for InAs QDs on MMB [31], and about 2.6 ns for InAs/InP QDs [32], while remaining below 1 ns for InGaAs/GaAs QDs and GaAs in nanoholes [7, 18]. Under phonon-assisted two-photon excitation, the lifetimes of the exciton and biexciton for InAs QDs grown on MMB [33] were found to be 1.256 ns and 446 ps respectively, while 259 ps and 120 ps were measured for GaAs QDs in nanoholes [34]. On the other hand, commercial InGaAs cameras commonly used at these wavelengths, offer higher quantum efficiency but typically have lower resolution and suffer from higher electronic noise compared to Si cameras operating at shorter wavelengths. The dark current is larger by at least four orders of magnitude depending on the cooling temperature [35, 36], making the detection of low-intensity signals more challenging. Nonetheless, wide-field imaging of 1550 nm QDs has been recently demonstrated with a thermo-electrically cooled InGaAs camera [36].

Here, we present the PL mapping of telecom C-band QDs by confocal laser scanning microscopy. In addition to obtaining the spatial coordinates of the emitter, the emission wavelength of the collected photons can be simultaneously determined by a spectrometer with a linear InGaAs photodiode array (PDA). When the full spectrum is not required, the signal can be filtered with a narrow bandpass filter and recorded with a superconducting nanowire single-photon detector (SNSPD), allowing a faster acquisition and an enhanced detection of weak emitters. Besides, we detail a numerical procedure to obtain the coordinates of the QDs from a recorded PL map. We also consider the distortion of the acquired maps, which can result from various imperfections in the scanning system. First, geometric deformations can arise if the optical beams do not impinge on the center of the scanning mirror [37]. Perspective distortion may also occur if the sample plane is not perfectly perpendicular to the objective optical axis [38], and barrel or pincushion distortions can be caused by an aperture within the optical system [38]. Distortions were largely overlooked by previous studies [36, 39, 40], assuming their impact was negligible. However, the QD positions found with the imaging system can be misleading, since even imperceptible distortions can significantly shift the actual positions of the QDs on the acquired maps. With our method applied on a moderately bright QD located within a 390×390 pixel PL map acquired over a 10.5 h period, we obtain a positioning uncertainty below 15 nm when neglecting distortions. After distortion correction, we find that the previously determined position is shifted by 303 nm compared to the corrected QD position, underlining the need for distortion corrections. The positioning uncertainty then increases to about 155 nm after correction due to error propagation. For lower resolution maps (240×230 pixels), we find that 10% of the QDs can be located with an uncertainty of 11 nm and 110 nm before and after correction of distortions, respectively. On average, the image distortion introduced a 428 nm shift on the QD positions.

2. Materials and methods

The sample investigated is grown by metal-organic vapor-phase epitaxy (MOVPE) on a Si-doped (100) GaAs substrate. The heterostructure consists of a 19.5 pairs of AlAs/GaAs (134.4 nm/ 114.6 nm) distributed Bragg reflector, a 1150 nm $In_xGa_{1-x}As$ MMB layer with indium content gradually increased from $x = 0.015$ to $x = 0.4$, active InAs QDs and a 205 nm $In_{0.3}Ga_{0.7}As$ capping layer. The presence of the MMB layer relaxes the lattice strain on the QDs [33, 41], which increases their lateral size and shifts their emission wavelength to 1550 ± 20 nm. The QD density is estimated by atomic force microscopy on a similar uncapped sample to be approximately 3.9×10^9 cm^{-2}, which corresponds to a mean QD separation of 160 nm. The average diameter for QDs with heights below 10 nm is 47 nm. A 5 × 5 grid made of Ti (5 nm) and Au (80 nm) is patterned on the surface by EBL and lift-off. The metal stripes are 3 μm wide and the pitch between two square unit cells is 23 μm.

As shown in figure 1(a), the sample is mounted on *xyz* nanopositioner stages inside a cryostat equipped with a fixed cryogenic objective ($NA = 0.77$). In our scanning approach, the QDs are quasi-resonantly excited into the *p*-shell through the objective with a pulsed laser at 1470 nm (80 MHz repetition rate) coupled to a single mode fiber. The signal collected by the same objective is coupled to a second single mode fiber and either directed to the spectrometer or to the SNSPD. With this confocal arrangement, better spatial resolution can be obtained compared to the wide-field approach.

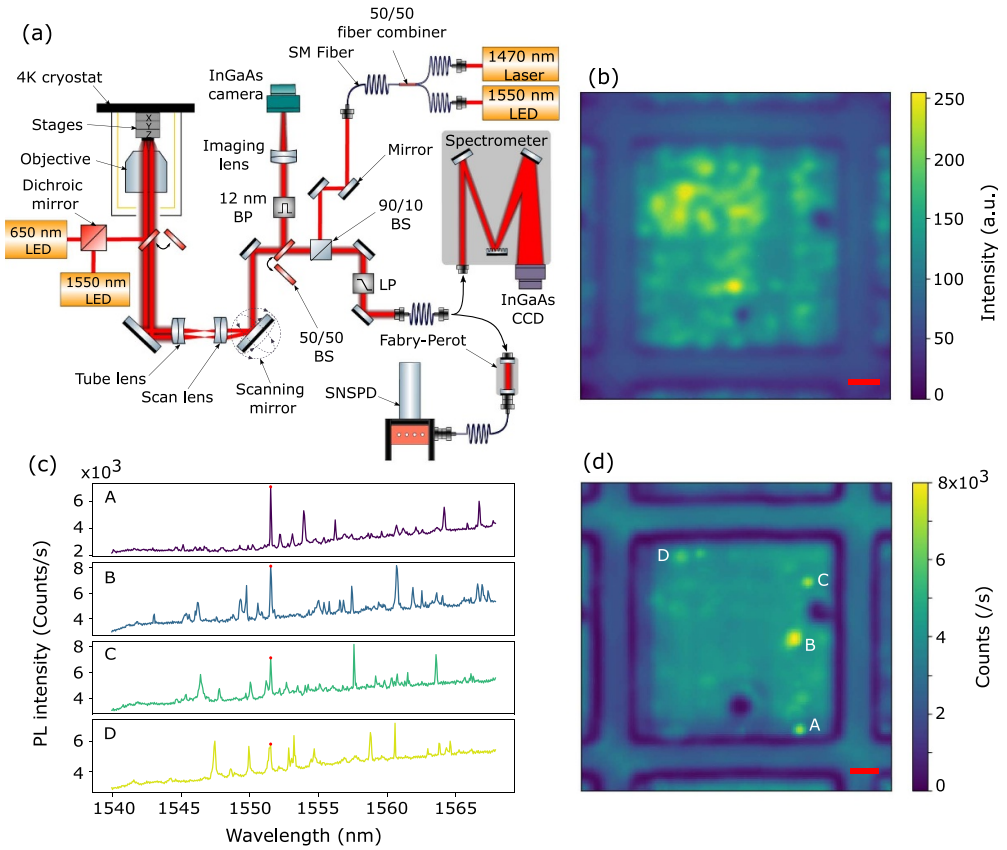

Figure 1. (a) Sketch of the confocal laser scanning microscope and wide-field imaging system. (b) Wide-field PL image of the sample after filtering with a (1550 ± 6) nm bandpass. The exposure time was set to 6 s. The two dark spots on the image correspond to two metal markers used to label the unit cell. (c) Four PL spectra showing the emission line (red dot) of the QDs emitting at 1551.6 nm and labeled A, B, C and D in (d). The QDs were excited by the laser and the signal recorded with the InGaAs PDA consists of the diffracted PL signal together with reflected light incoherent light. (d) PL map at 1551.6 nm of the previous unit cell obtained by scanning and by recording the diffracted signal with the InGaAs sensor. For the two images, the scale bar is 3 μm and distortions have been corrected.

The excitation and detection beams can be deflected in steps by a dual-axis scanning mirror with a high angular resolution (22 μrad) and good repeatability (40 μrad), allowing to perform PL mapping. A scanning lens ($f = 50$ mm) and a tube lens ($f = 150$ mm) are inserted between the scanning mirror and the objective to form a 4-f optical system. The objective is designed to be apochromatic between 1170 and 1580 nm, and the scanning and tube lenses are achromatic over the same wavelength range, but we limit our mapping to the emission range of our QDs. In order to further minimize chromatic aberrations, the QDs are excited quasi-resonantly. To simultaneously image the metal grid, used as a reference for alignment, a fiber-coupled incoherent light source emitting (LED at 1550 nm with 50 nm bandwidth) is added in the excitation path with a fiber combiner. This configuration ensures that the spots of these two signals perfectly overlap on the surface of the sample. After filtering the excitation laser with a long pass filter, the detected signal then consists of the QD PL signal together with the incoherent light reflected by the alignment marks and the surface. The choice of the emission wavelength for the LED ensures that both the PL signal and the reflected incoherent light share at the same focal point. By comparing the reflectance of gold with InGaAs at 1550 nm, the markers are expected to be approximately three times brighter than the bare surface. The use of an incoherent light source is necessary to avoid diffraction patterns at the edges of the grid, which simplifies its detection. We estimate the spot size to be close to the Rayleigh diffraction limit. Assuming uniform illumination of the objective, the resulting lateral resolution of the scanner is therefore $d = 0.61 \cdot \lambda / NA \approx 1.23\,\mu$m, which is smaller than the width of the metal strips and ensures their identification. To compare with our scanning-based imaging, a wide-field image of the surface can also be obtained with an InGaAs SWIR camera (1280 × 1024 pixels chip) thermo-electrically cooled to 10 °C. The QDs are then off-resonantly excited with a 650 nm LED, and the metal grid is imaged by reflection of 1550 nm light generated by a free-space LED. The signal is filtered with a (1550 ± 6) nm bandpass filter and then focused with a lens to fill the camera sensor area with a ×150 magnification.

3. Results

3.1. Wavelength resolution

One unit cell of the grid and the QDs are initially imaged by wide-field microscopy with the camera in a single acquisition (6 s), as shown in figure 1(b) in gray-scale. By reflecting the 1550 nm LED light, the gold metal strips are distinct from

the InGaAs surface, despite being approximately 40% darker. This effect is due to the background PL emission of our sample [41], whose intensity is comparable to that of the reflected 1550 nm light. The choice of LED intensity and integration time is a compromise between three desirable features of the image: the grid imaged by reflection with a good contrast, the PL signal of the QDs [33] not masked by the reflected signal and the pixels not being saturated. With the current configuration found as optimal, the signal of the QDs is larger than that of the InGaAs surface by factor between 1.3 and 2, depending on the brightness of the QD. A larger contrast could in principle be achieved by imaging a sample without background emission in the spectral range of interest. The edges of the grid exhibit a slight blurring due to the large diffraction-limited spot size and are clearly discernible by an intensity dip caused by scattering, which is a beneficial feature for localization. Specifically, the inner of the metal strips and the InGaAs surface are brighter than the edges by factors of about 1.3 and 2.1, respectively. The noise level of the camera constitutes 1% of the grayscale, resulting in a PL signal to camera noise around 10 for QDs with an average brightness. At this level, the emitters can be localized with good accuracy [36]. To get more insight on the spectral properties of QDs detected by the camera, PL spectra can be acquired by locally exciting with the laser and measuring the dispersed PL signal with the PDA, as shown in figure 1(c). As a consequence of the high density of QDs, the spectra consist of numerous lines originating from multiple QDs excited within the laser spot area. Therefore, the majority of the spots captured by the camera likely stem from clusters of QDs rather than individual ones, even when employing the 12 nm bandwidth filter. In principle, this effect can be mitigated by reducing the bandwidth of the filter to 1 or 2 nm. However, the signal-to-noise ratio will decrease to the extent that individual emitters can no longer be localized efficiently. We note that a more sophisticated camera with a better cooling system to lower the noise level may alleviate this issue, but imaging dim emitters will remain challenging.

An image of the same unit cell was also obtained by confocal laser scanning microscopy. The signal was recorded with the spectrometer and the liquid nitrogen-cooled InGaAs PDA. At each step, PL spectra were recorded with a 55 pm wavelength resolution within a 28 nm range. Despite the longer acquisition time (7 h for a 160 × 160 pixels image), the emission wavelength and the position of the QDs can be simultaneously recorded. Figure 1(d) depicts only the QDs emitting at 1551.6 nm which are well-isolated by the narrow filtering. The lineshape can also be investigated from the PL spectra, as shown in figure 1(c). The QD 'A' exhibits the desirable sharp and isolated emission line and previous studies [27, 33] on the same type of QDs demonstrated that it can be a promising single photon source. The emission lines of the other labeled QDs are broader and may overlap with adjacent lines, which would likely not be considered for integration. With the chosen intensity of the LED signal, the intensity of the reflected light on InGaAs surface is larger by a factor of about 5.8 than that measured at the edges of the marker. Similarly, this factor is about 4.9 between the inner part of the markers and their edges. With the background level of the camera being as low as 50 counts s^{-1}, the QD can be detected with a signal-to-noise ratio around 150. Since the count rate is below saturation (6.5×10^4 counts s^{-1}), the LED intensity could be increased further to enhance the contrast between the grid and the surface without compromising the contrast between the QDs and the surface. The better performances in terms of spectral filtering while achieving a higher contrast and significantly larger signal-to-noise ratio demonstrate the viability of the scanning approach to localize telecom QDs.

3.2. *Procedure to locate the QDs*

To detail our methodology for QD localization, we consider one unit-cell as shown by the scanning electron microscopy (SEM) image in figure 2(a). The patterned EBL grid does not exhibit discernible deformations that could have occurred during writing, as confirmed by inspection under the SEM. Henceforth, we proceed with the assumption that the imaged grids match the EBL pattern file. A high-resolution grayscale PL scan (390×390 pixels, corresponding to angular steps of 0.0023°) of this unit cell was acquired, as shown in figure 2(b). The signal was filtered at (1550 ± 0.5) nm with a fiber Fabry–Perot and detected with an SNSPD. Photons were counted for 100 ms by the built-in driver of the detector and recorded by the control computer at each scanning step (communication delay of 150 ms). Compared to the previous detection method with the spectrometer, the scanning speed is increased by a factor of five and the narrow filtering still allows for the identification of QDs with non-overlapping emission profiles. However, the contrast between the metal strips and the surface is insufficient to accurately identify the edges. Therefore, the power of the LED signal at 1550 nm was increased, as shown in figure 2(c). The QDs remain easily discernible above the reflected light background. The morphology of the surface, characterized by a cross-hatch pattern typical of heterostructure with a MMB [42, 43], also becomes apparent. Some faint shadows of edges can be seen due to instrument aberrations, but this artifact does not affect the image analysis. The horizontal line-cut (figure 2(e)) reveals that the edges of the strip are darker by at least a factor 3 and 5 compared to the inner section of strip and the InGaAs surface, respectively. Despite the reflected background, the amplitude of the QDs highlighted still represents between 15% and 23% of the grayscale intensity of the map.

The strategy to locate the QDs consists in first finding the four inner and outer edges of the grid with multiple horizontal or vertical line-cuts. For each of them, the minimum of the intensity dip at the edge is fit with a gaussian function with the least-squares method. The FWHM of the fitted profile is on average 940 nm for the four edges in the line-cut shown in figure 2(e). The middle distance between the inner and outer edges is then linearly fitted with a slope s_i and intercept r_i by least-squares method ($i = 1,..,4$ for the four strips). The curved edges near the crosses are avoided

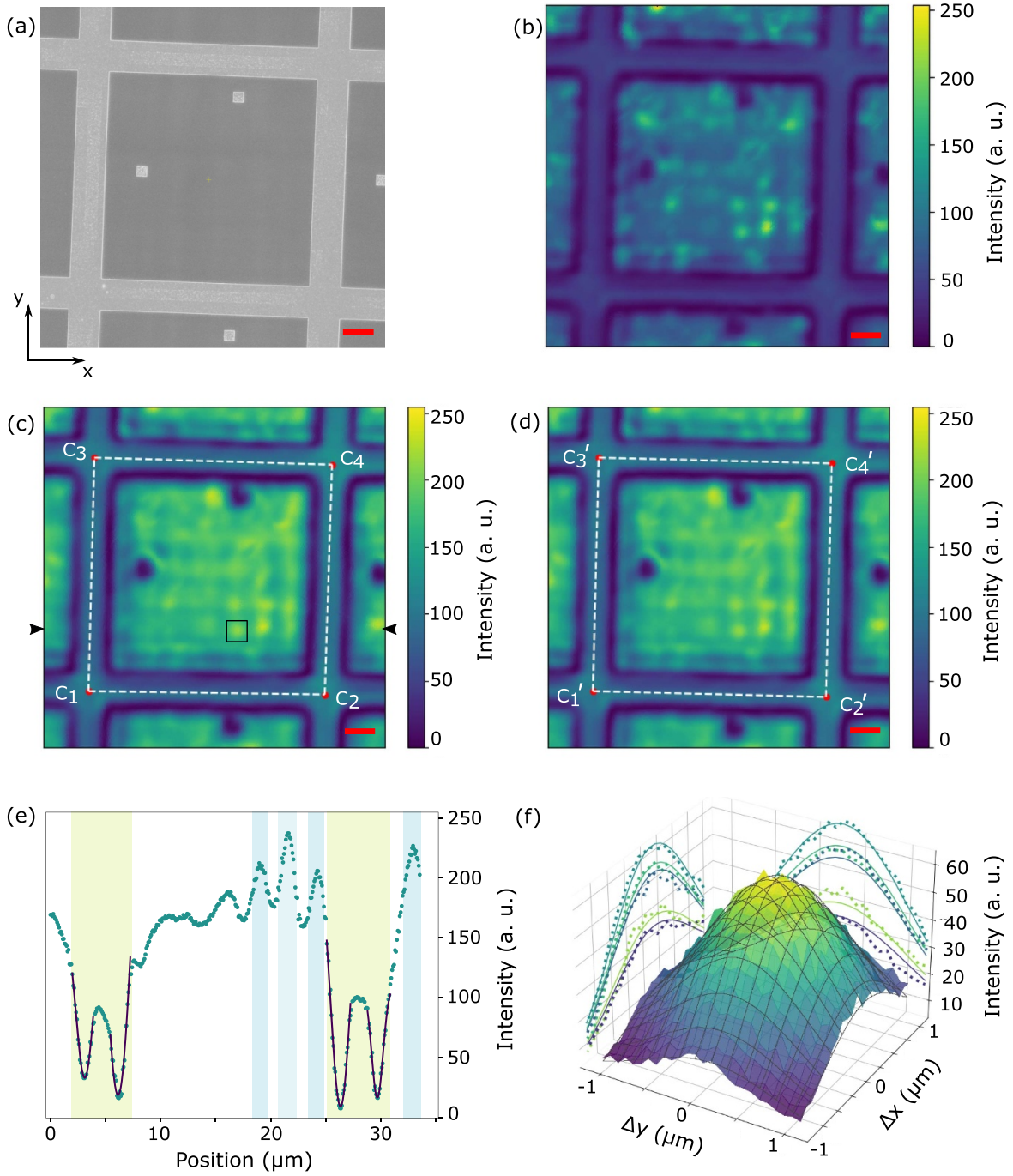

Figure 2. (a) SEM image of the investigated unit cell. The scale bar is 3 μm for the SEM image and the PL maps. (b) Grayscale PL image acquired by scanning and recording the signal with a fiber Fabry–Perot and an SNSPD. The whole acquisition took 10.5 h. (c) Same PL map acquired with more incoherent light at 1550 nm to enhance the reflected signal on the metal strips. The dashed white lines indicate the center of the metal strips obtained after edge detection. The pixel size is 86.2 nm, calculated from the distance between the corners $\mathbf{C_1}$ and $\mathbf{C_3}$. (d) PL map after perspective transform correction. (e) Horizontal line-cut at the position indicated by the two arrows in the map. The green and blue regions highlight the metal strips and bright QDs, respectively. The edges of the metal strip are found by gaussian fitting. (f) Fitting of the QD indicated by the black square in (c) by an elliptical gaussian distribution. The FWHM are $\approx$ 732.8 nm and $\approx$ 659.6 nm along the *x*-axis and *y*-axis, respectively.

for better accuracy. The intersections of the four lines provide the four corners of the grid $\mathbf{C_i} = (C_{i,x}, C_{i,y})$, forming a basis to locate the QDs. Finally, the QD centers are found by fitting their emission profile with an elliptical gaussian function, as depicted in figure 2(f). For a QD with average brightness, boxed in figure 2(c), the fitting standard error on the position of the center is $\sigma_{\mathrm{QD},x} = 3.6$ nm and $\sigma_{\mathrm{QD},y} = 3.3$ nm ($\sigma_{\mathrm{QD}} = \sqrt{(\sigma_{\mathrm{QD},x})^2 + (\sigma_{\mathrm{QD},y})^2} = 4.8$ nm).

A close inspection of the scanned PL map reveals a distortion of the detected grid, stemming from aberrations introduced by the imaging system. Typically resulting from a combination of multiple causes such as imperfect alignment, placement and specifications of the optical components, the aberrations can be minimized but never completely eliminated. A shearing, an elongation or a combination of both in the image could also originate from a linear drift of the sample inside the cryostat during acquisition. However, we could repeat the same deformation as observed in figure 2(c) by running a faster map, which indicates that it is primarily introduced by the scanner. These distortions modify the positions of the corners and the QDs on the map and have to be corrected to obtain accurate coordinates.

In our correction process, we consider both linear transformations (rotation, scaling, shearing and translation) and non-orthogonal transformations (perspective) [44]. Given the small angles scanned by the mirror and therefore the scan field of view, we approximate higher order effects like barrel and pin-cushion to a perspective deformation on the scale of the acquired map. For each point of the map, the corrected coordinates $\mathbf{X}' = (x', y')$ are found from the 3×3 perspective matrix $\mathbf{P}$ and the distorted coordinates $\mathbf{X} = (x, y)$ as:

$$\begin{pmatrix} tx' \\ ty' \\ t \end{pmatrix} = \begin{pmatrix} a_1 & a_2 & a_3 \\ a_4 & a_5 & a_6 \\ a_7 & a_8 & 1 \end{pmatrix} \begin{pmatrix} x \\ y \\ 1 \end{pmatrix}. \quad (1)$$

The coefficients of the matrix $\mathbf{P}$ are derived by solving the system of 8 equations, which maps the coordinates of the four distorted corners $\mathbf{C_i}$ to the corners $\mathbf{C_i'}$ of an ideal unit cell. To construct the latter, we choose the two corners found with the smallest error as invariant (C_1 and C_3), while the other two are geometrically constructed. Other constructions are possible: the resulting map would then differ by a rotation and scaling factor, but the QD position after correction would remain the same in the reference frame of the corrected corners. While identifying four corners in the distorted map is required to define the perspective transformation, finding the distance of the QD with respect to two corrected corners is sufficient to know its position, and knowing its distance to the two other corners will not enhance the accuracy. Figure 2(d) shows the PL map after correction, and the disparities with the uncorrected map are hardly noticeable. The QD positions are corrected by applying the perspective transform (equation (1)) to the distorted coordinates as found in figure 2(f). In this case, the QD corrected position lies 298.0 nm and 53.7 nm away from its originally found position, in the x- and y- directions respectively, which corresponds to a total distance of 302.8 nm. Compared to photonic structures typically on the scale of 1 to 2 μm, these values are significant and thus emphasize the need for correcting the distortions in order to obtain a good alignment.

3.3. Uncertainty on the position

For each of the four lines fitting the middle of the fours strips, we write $\sigma_{s,i}$ and $\sigma_{r,i}$ the fitting standard errors of the slope and intercept, respectively. Since the lines were detected separately and away from the corners, the uncertainties on the slopes and intercepts are uncorrelated. The coordinates of the corners $\mathbf{C_i}$ are found by solving the linear system of two intersecting lines, and we write $\boldsymbol{\sigma}_{C_i} = (\sigma_{C_{i,x}}, \sigma_{C_{i,y}})$ the uncertainty on their positions. By error propagation, they are expressed as:

$$\sigma_{C_i,x} = \sqrt{\sum_n \left[\left(\frac{\partial C_{i,x}}{\partial s_n} \sigma_{s,n} \right)^2 + \left(\frac{\partial C_{i,x}}{\partial r_n} \sigma_{r,n} \right)^2 \right]}, \quad (2)$$

where n corresponds to the index of the two lines used to find the corner $\mathbf{C_i}$. A similar expression is found for the y-coordinate of the corners. The full form equations are derived analytically with Wolfram Mathematica and the numerical values can be subsequently computed. We define the error on the position of the corner as $\sigma_{C_i} = \sqrt{(\sigma_{C_{i,x}})^2 + (\sigma_{C_{i,y}})^2}$, which lays between 13.2 nm and 56.8 nm depending on the corner. Without correcting the distortion, the error on the position of the QD with respect to one of the corners [40] is then $\sigma_{\mathrm{QD}+C_i} = \sqrt{(\sigma_{\mathrm{QD}})^2 + (\sigma_{C_i})^2}$, which is equal to 14.0 nm by choosing the corner C_3 found with the smallest error.

By correcting the distortion of the image, the error on the position of the distorted corners $\mathbf{C_i}$ must be propagated to the perspective transform $\mathbf{P}$. The positions of the destination corners $\mathbf{C_i'}$ are by definition ideal and do not bear any error. The uncertainty of the coefficients a_i is then calculated by:

$$\sigma_{a_i} = \sqrt{\sum_{i=1}^{4} \left[\left(\frac{\partial a_i}{\partial C_{i,x}} \sigma_{C_{i,x}} \right)^2 + \left(\frac{\partial a_i}{\partial C_{i,y}} \sigma_{C_{i,y}} \right)^2 \right]}. \quad (3)$$

Finally, the uncertainty $\boldsymbol{\sigma}_X' = (\sigma_{x'}, \sigma_{y'})$ on the corrected position $\mathbf{X}'$ of each point of the map is given by:

$$\sigma_{x'} = \sqrt{\sum_{i=1}^{8} \left[\left(\frac{\partial x'}{\partial a_i} \sigma_{a_i} \right)^2 \right] + \left(\frac{\partial x'}{\partial x} \sigma_x \right)^2 + \left(\frac{\partial x'}{\partial y} \sigma_y \right)^2}, \quad (4)$$

where $\boldsymbol{\sigma}_X = (\sigma_x, \sigma_y)$ is the uncertainty of the location of a point in the distorted map. A similar equation is found for $\sigma_{y'}$. The propagation of errors for the QD located in figure 2(c) gives $\sigma_{\mathrm{QD},x'} = 123.4$ nm and $\sigma_{\mathrm{QD},y'} = 93.8$ nm ($\sigma_{\mathrm{QD}'} = \sqrt{(\sigma_{\mathrm{QD},x'})^2 + (\sigma_{\mathrm{QD},y'})^2} = 155.0$ nm and $\sigma_{\mathrm{QD}'} = \sigma_{\mathrm{QD}'+C_3'}$ since there is no error in the position of C_3'). These values, significantly larger than that obtained before corrections, show that the distortion is the dominant source of errors in our mapping technique. To contextualize these errors, we simulated by Finite-Difference Time-Domain (figure 3(a)) the enhancement in collection efficiency at 1550 nm provided by

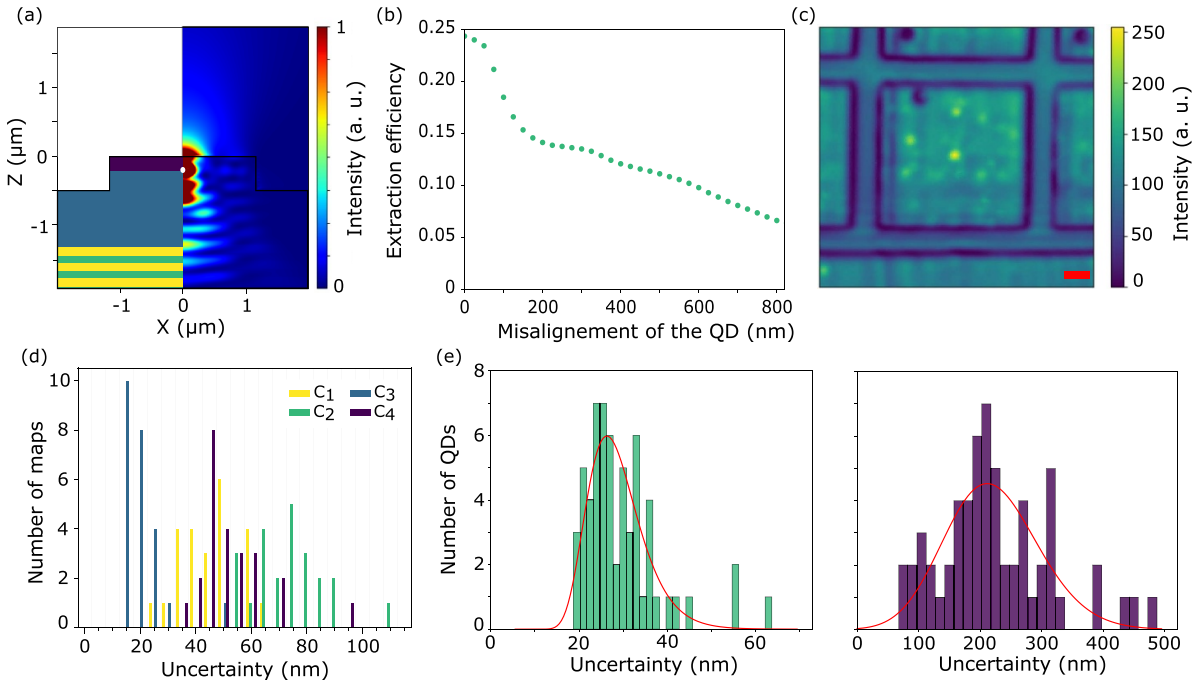

Figure 3. (a) Electric field intensity (E^2) profile of a pillar etched (diameter 2.3 μm and height 500 nm) in the sample (purple: capping layer, blue: metamorphic buffer, yellow: AlAs, Green: GaAs). (b) Influence of the misalignment QD/pillar on the collection efficiency. (c) Example of a 240 × 230 pixels grayscale PL image as acquired. The scale bar is 3 μm. (d) Histogram of the errors on the location of the four corners. The orientation of all maps remains consistent, with the labeling of the four corners following the convention established in figure 2. (d) Histogram of the error on the QDs position located in the 24 grids before (left) and after (right) correction of distortions, fitted by a log-normal distribution (red line).

etching a pillar (diameter 2.3 μm and height 500 nm) in our sample. A perfectly aligned QD with the center of the pillar results in a 23% collection efficiency by the microscope objective. As illustrated in figure 3(b), the design proves resilient to a misalignment below 80 nm which lays within the capabilities of our scanner in the absence of distortions, but a shift of around 155 nm would degrade the performance down to 14%.

4. Discussion

In contrast to previous studies employing wide-field imaging, our confocal laser scanner can provide the PL spectra of the mapped QDs, allowing to spatially and spectrally couple them to fabricated photonic structures. To compare our alignment accuracy, and specifically with emitters at 1550 nm, we note that an uncertainty below 80 nm for 10% of the emitters has been demonstrated with wide-field imaging [36]. Our mapping technique reaches an even lower level, assuming a perfectly aligned scanner. Yet, we find that the correction of distortions, even visually imperceptible, can significantly increase the final uncertainty by error propagation. An even more precise adjustment of our instrument will noticeably help to minimize distortions. We also conducted a more in-depth analysis of the effects of distortions which are, to the best of our knowledge, neglected in earlier works. For QDs emitting below 1 μm, marker-based PL imaging locates the QDs with uncertainties below 10 nm, but offsets between the QD and the fabricated photonic structure are often measured up to 100 nm even after subtraction of the error introduced by EBL [40]. The quality of the marker and the fitting method may contribute to this discrepancy, but a deformation of the whole image such as a perspective or a barrel/pin-cushion could also have an impact at such a small scale. The better performance of *in-situ* EBL [26], where the photonic structure is directly fabricated on the QD without the need of marker-based positioning, also hints towards detrimental effects of distortions.

To demonstrate the repeatability of both the mapping and the analysis approach described above, QDs were located over 24 unit cells distributed across the chip. The angular stepsize was changed to 0.0040° for faster acquisition of 240×230 pixels PL maps, as shown in figure 3(c). A degradation of the positioning accuracy compared to the higher resolution map in figure 2(c) is therefore expected due to the larger pixel size, but this does not influence the positioning error distribution. The histogram of the error σ_{C_i} on the position of the four corners (figure 3(d)) indicates that the mean error varies with the corner fitted, from 22.8 nm for the top left corner to 78.0 nm for the bottom right corner. This systematic difference can be attributed to a change of contrast at the edges of the metal strips, possibly due to a tilt of the sample. On this set of PL maps, QDs were located prior to any processing, and then mapped to their distortion-free positions. On average, we obtain a shift in their position of 427.9 nm, underscoring the importance of the distortion correction procedure. Figure 3(e) depicts the distribution of the uncertainty on their position $\sigma_{\mathrm{QD}+C_3}$ and $\sigma_{\mathrm{QD}'}$ before and after the distortion correction,

respectively. The uncertainty profiles can be best fitted with a log-normal distribution, and we obtain a median error of 27.9 nm and 216.5 nm, respectively. We find that 10% of the QDs have an uncertainty below 11 nm and 110 nm, respectively. The spread of the uncertainty distributions can stem from various factors, including the proximity of the surface to the focal plane of the objective, the brightness of the QD, the severity of the distortion at the QD location or the presence of weak neighboring emitters affecting the spatial profile.

We expect that a better positioning accuracy of the scanner can be obtained by imaging a sample without any background emission at telecom wavelength, as well as by improving the alignment accuracy which would reduce the amount of distortions. Indeed, the scanning mirror could be mounted on translation stages to ensure that the optical beams impinge on its center in order to avoid geometric distortions. Similarly, the scan and tube lenses could also be mounted on translation stages to improve the 4-f system. If space allows, increasing the focal lengths of the lenses and thus increasing their radii of curvature would minimize spherical aberrations. Finally, a perspective effect can occur if the sample plane is not perpendicular to the optical axis of the objective. This could be compensated for by inserting tilting stages on top of the *xyz* stack in the cryostat.

Further improvements of the scanning microscope can be envisioned. Pumping the QDs above-band within the achromatic range of the optics would reduce the laser excitation spot size, thereby decreasing the lateral size of the QDs in the images. This reduction could potentially minimize the overlap between neighboring QDs and enhance the fitting accuracy. In terms of scanning speed, the photon counts could be continuously recorded along with trigger signals generated by the scanning mirror at each step by a fast counting card. The resulting PL map would only be retrieved at the end of the acquisition. This scheme would suppress the communication delay at each step, reducing the acquisition time of the PL maps presented above by a factor 2.5, increasing the throughput of our system. This reduction would also be advantageous since the map acquisition would become more robust against potential sample drift. Thereafter, the reflected signal around 1550 nm used for marker identification could be separated from the PL signal of the sample by a narrow-band notch filter at the emission wavelength of interest of the QDs and placed after the longpass filter. In this configuration, one avalanche photodiode or SNSPD would detect the reflected signal while another one would detect the PL signal further filtered by the Fabry Perot at a wavelength inside of the notch filter bandwidth. With such a setup, the intensity of the 1550 nm LED used to image to the metal strips can be increased without raising the overall background of the map.

5. Conclusion

In conclusion, we used confocal laser scanning microscopy for both spatial localization and spectral characterization of QDs emitting in the telecom C-band. This approach isolates and locates dense and dim emitters within a narrow spectral bandwidth, with a better contrast and signal-to-noise ratio than the wide-field imaging technique. Our method demonstrates an alignment uncertainty below 11 nm for 240×230 pixel maps for 10% of the QDs, in the absence of distortions of the image. Yet, we found that the QD positions in the as-acquired PL maps were shifted by 428 nm on average compared to their corrected positions due to optical distortions in our system. After distortion correction and error propagation, the final uncertainty increases to 110 nm. This non-negligible shift underlines the need to consider the detrimental effects of distortions for accurate positioning, given their unavoidable occurrence in any optical system. Fabrication of photonic structures such as micro-pillars and micro-lenses which tolerate our current alignment error is already possible with our scanner capabilities. We anticipate that an even finer alignment to reduce aberrations of the system will enhance the final accuracy, enabling fabrication of more sophisticated devices based on photonic cavities or circular Bragg gratings.

6. Author contributions

Conceptualization, T D and V Z; methodology, T D and A B; formal analysis, T D, A B and M Huet; investigation, T D, A B and M Huet; resources, M Hammar; data curation, T D, A B, M Huet; writing—original draft preparation, T D; writing—review and editing, T D, A B, M Huet, M.Hammar and V Z; supervision, T D and V Z; funding acquisition, V Z

Data availability statement

All data that support the findings of this study are included within the article (and any supplementary files).

Acknowledgments

This research was funded by the Swedish Research Council (VR) Grants (Reference 2023-04604; 2023-05663; 2020-04861).

ORCID iD

Thomas Descamps https://orcid.org/0009-0005-6875-5009

References

[1] Basset F B *et al* 2021 *Sci. Adv.* **7** 6379
[2] Zhai L, Nguyen G N, Spinnler C, Ritzmann J, Löbl M C, Wieck A D, Ludwig A, Javadi A and Warburton R J 2022 *Nat. Nanotechnol.* **17** 829–33
[3] Heindel T, Kim J H, Gregersen N, Rastelli A and Reitzenstein S 2023 *Adv. Opt. Photon.* **15** 613
[4] Moody G *et al* 2022 *J. Phys. Photon.* **4** 012501
[5] Castelletto S and Boretti A 2023 *Adv. Quantum Technol.* **6** 2300145
[6] Schweickert L *et al* 2018 *Appl. Phys. Lett.* **112** 93106
[7] Schöll E *et al* 2019 *Nano Lett.* **19** 2404–10

[8] Müller T, Skiba-Szymanska J, Krysa A B, Huwer J, Felle M, Anderson M, Stevenson R M, Heffernan J, Ritchie D A and Shields A J 2018 *Nat. Commun.* **9** 1–6
[9] Yu Y, Liu S, Lee C M, Michler P, Reitzenstein S, Srinivasan K, Waks E and Liu J 2023 *Nat. Nanotechnol.* **18** 1389–400
[10] Hepp S, Jetter M, Portalupi S L and Michler P 2019 *Adv. Quantum Technol.* **2** 1900020
[11] Carter S G, Sweeney T M, Kim M, Kim C S, Solenov D, Economou S E, Reinecke T L, Yang L, Bracker A S and Gammon D 2013 *Nat. Photon.* **7** 329–34
[12] Wang H *et al* 2019 *Nat. Photon.* **13** 770–5
[13] Doughty G, Thoms S, Law V and Wilkinson C 1986 *Vacuum* **36** 803–6
[14] Varoutsis S, Laurent S, Laurent S, Sagnes I, Lemaître A, Ferlazzo L, Mériadec C, Patriarche G, Robert-Philip I and Abram I 2005 *J. Vac. Sci. Technol.* B **23** 2499–503
[15] Krieger T M *et al* 2024 *ACS Photonics* **11** 596–603
[16] Albert F *et al* 2013 *Nat. Commun.* **4** 1–6
[17] Liu J *et al* 2018 *Phys. Rev. Appl.* **9** 064019
[18] Dalgarno P A, Smith J M, McFarlane J, Gerardot B D, Karrai K, Badolato A, Petroff P M and Warburton R J 2008 *Phys. Rev.* B **77** 245311
[19] Warburton R J 2013 *Nat. Mater.* **12** 483–93
[20] Sautter K E, Vallejo K D and Simmonds P J 2020 *J. Appl. Phys.* **128** 031101
[21] Sutula M *et al* 2023 *Nat. Mater.* **22** 1338–44
[22] Liu J, Davanço M I, Sapienza L, Konthasinghe K, De Miranda Cardoso J V, Song J D, Badolato A and Srinivasan K 2017 *Rev. Sci. Instrum.* **88** 023116
[23] Liu S *et al* 2023 arXiv:2311.02626
[24] Thon S M, Rakher M T, Kim H, Gudat J, Irvine W T, Petroff P M and Bouwmeester D 2009 *Appl. Phys. Lett.* **94** 111115
[25] Dousse A, Lanco L, Suffczyński J, Semenova E, Miard A, Lemaître A, Sagnes I, Roblin C, Bloch J and Senellart P 2008 *Phys. Rev. Lett.* **101** 267404
[26] Rodt S and Reitzenstein S 2021 *Nano Express* **2** 014007
[27] Zeuner K D *et al* 2018 *Appl. Phys. Lett.* **112** 173102
[28] Vajner D A *et al* 2024 *ACS Photonics* **11** 339–47
[29] Huo Y H, Rastelli A and Schmidt O G 2013 *Appl. Phys. Lett.* **102** 152105
[30] Huber D, Reindl M, Aberl J, Rastelli A and Trotta R 2018 *J. Opt.* **20** 073002
[31] Nawrath C *et al* 2023 *Adv. Quantum Technol.* **6** 2300111
[32] Holewa P *et al* 2022 *ACS Photonics* **9** 2273–9
[33] Zeuner K D *et al* 2021 *ACS Photonics* **8** 2337–44
[34] Reindl M, Jöns K D, Huber D, Schimpf C, Huo Y, Zwiller V, Rastelli A and Trotta R 2017 *Nano Lett.* **17** 4090–5
[35] Chen Y, Spinelli S and Pan Z 2024 *J. Mater. Chem.* **12** 7542–51
[36] Holewa P *et al* 2023 *Nat. Commun.* **15** 1–9
[37] Yan C, Shi Y, Zhaoqing L, Wen S and Wei Q 2020 *Selective Laser Sintering Additive Manufacturing Technology* (Academic)
[38] Pedrotti F L, Pedrotti L M and Pedrotti L S 2017 *Introduction to Optics* 3rd edn (Cambridge University Press)
[39] Sapienza L, Davanço M, Badolato A and Srinivasan K 2015 *Nat. Commun.* **6** 1–8
[40] Madigawa A A *et al* 2023 *ACS Photonics* **11** 1012–23
[41] Paul M, Olbrich F, Höschele J, Schreier S, Kettler J, Portalupi S L, Jetter M and Michler P 2017 *Appl. Phys. Lett.* **111** 33102
[42] Sittig R *et al* 2022 *Nanophotonics* **11** 1109–16
[43] Andrews A M, Speck J S, Romanov A E, Bobeth M and Pompe W 2002 *J. Appl. Phys.* **91** 1933–43
[44] Zeng Z 2022 Towards an optical interface to spin qubits *PhD Thesis* RWTH Aachen University